



Efficient degradation of organic pollutants by enhanced interfacial internal electric field induced via various crystallinity carbon nitride homojunction

Yan Guo^{a,b}, Sijie Huang^b, Yang Guo^b, Zhiqiang Ye^{b,c}, Jun Nan^a, Qixin Zhou^{b,*}, Yongfa Zhu^{b,*}

^a School of Environment, Harbin Institute of Technology, Harbin 150090, China

^b Department of Chemistry, Tsinghua University, Beijing 100084, China

^c School of mechanical Engineering, Yancheng Institute of Technology, Yancheng 224051, China

ARTICLE INFO

Keywords:

Carbon Nitride

Homojunction

Degradation

Continuous-flow reactor

Photocatalysis

ABSTRACT

Herein, a homojunction carbon nitride photocatalyst integrated with three crystallization levels (Tri-crystallinity) is developed to enhance the degradation activity of organic pollutants. The increase in crystallinity induces the Fermi level and band position to decrease. This difference constructs an internal electric field (IEF) at the interface with a lower to higher crystallinity direction. The multiple contact interfaces in Tri-crystallinity reinforce the interfacial IEF twice compared to a conventional single-interface. The interfacial IEF improves charge separation and transfer, and the degradation of antibiotics by Tri-crystallinity carbon nitride is at least 20 times greater than primary carbon nitride. Further, the Tri-crystallinity carbon nitride loading on a nonwoven fabric in a continuous-flow reactor achieves 91.0% purification of the organic wastewater at a flow rate of 14.2 L h⁻¹ m⁻² from 11:00 a.m. to 3:00 p.m. This work provides a strategy for engineering interfacial IEF of future efficient photocatalysts.

1. Introduction

Antibiotics including Ofloxacin, Tetracycline, Ciprofloxacin, and Vancomycin are widely used for human health and livestock breeding [1–4]. As the conventional biological treatment process is challenging to treat antibiotic wastewater in the sewage treatment plant, antibiotic pollution is distributed in the environmental water [5]. Antibiotics cause bacteria to develop resistance, which threatens ecosystems. Advanced Oxidation Process (AOPs) is an effective technology for organic wastewater treatment. Photocatalysis has attracted attention since its oxidative destruction of organic pollutants, promising potential solar energy applications [6,7]. As a metal-free and sustainable photocatalyst, carbon nitride (CN) is attractive due to its easy synthesis and high chemical tunability [8,9]. However, the severe recombination of photogenerated electrons and holes restricts the degradation performance and stability, far from the industrial demand requirements. It is also noted that there are few reports of continuous-flow devices designed to obtain efficient degradation of organic pollutants using CN photocatalysts.

The internal electric field (IEF) in photocatalyst is a driving force for the separation and migration of photogenerated electron-holes pairs [10,11]. Tuning to obtain enhanced IEF results in the photocatalytic

performance improved [12]. Elemental doping builds up electron-rich centers [13,14] and modifies electron-rich groups [15] serve as effective strategies for enhancing IEF. Both anion- (e.g., O, P, S, F, and I) and cationic (e.g., Fe³⁺, Cu²⁺, K⁺, and Li⁺) doped CNs have been prepared but under severe preparation conditions [16–18]. For example, P-doped porous carbon nitride nanosheets were obtained via melamine and 2-aminomethyl phosphonic acid copolymerization, followed by thermal exfoliation [19]. The amount of doping and the degree of group modification were difficult to control, leading to potentially undesirable reproducibility [20,21].

Constructing heterojunctions and homojunction for CN has become practical ways to enhance the IEF of CN. Generally, the space charge region at the interface is accompanied by the interfacial IEF [22]. Compared with heterojunction, the reduced lattice mismatch and defects benefit from the components' homogeneity [23,24]. CN homojunction can be easily prepared by mixing different raw materials. Wang et al. reported a homojunction of graphite-phase carbon nitride between ordered and disordered regions [25]. However, the complicated synthesis limits its large-scale application in a realistic environment. Although g-C₃N₄ (bulk)/g-C₃N₄ (nanosheet) with glucose-modified melamine as a precursor has been reported [26], the type II

Abbreviations: IEF, internal electric field; CN, carbon nitride.

* Corresponding authors.

E-mail addresses: zqx20@mails.tsinghua.edu.cn (Q. Zhou), zhuyf@mail.tsinghua.edu.cn (Y. Zhu).

<https://doi.org/10.1016/j.apcatb.2022.121388>

Received 21 January 2022; Received in revised form 4 April 2022; Accepted 6 April 2022

Available online 14 April 2022

0926-3373/© 2022 Elsevier B.V. All rights reserved.

heterojunctions weakened the redox capacity. 2D and 3D morphologies of CN form 2D/3D homojunction recently. Nevertheless, due to the small contact interface formed by 2D and 3D, the interfacial IEF has the limited enhancement of the photogenerated charge separation performance. The degradation rate constant is only 0.0104 min^{-1} for tetracycline hydrochloride [27]. We prepare CN homojunction retaining the strong oxidation and reduction potentials by simple one-pot calcination, providing a basis for large-scale water purification treatment.

Herein, a Tri-crystallinity CN homojunction with three crystallinities was proposed. Due to the Fermi levels gap between the CNs of different crystallinity, the enhanced IEF is obtained at the interfaces formed by pairs of three materials. Specifically, the IEF acts as a driving force of photogenerated carrier migration, effectively inhibiting charge recombination. Followed by the reactive oxygen species and holes increased, results in enhanced degradation activity. Moreover, the satisfactory degradation activity of Tri-crystallinity CN in extensible continuous-flow units shows a broad industrial application prospect.

2. Experimental section

2.1. Materials

Urea (99%, Aladdin, China), thiourea (99%, Aladdin, China), melamine (99%, Aladdin, China), dimethylpyridine N-oxide (DMPO, 99%, Sigma, USA), Tetracycline hydrochloride (TC, 99%, Sigma, US), Rhodamine B (99%, Aladdin, China), ciprofloxacin (CIP, 99%, Sigma, US), ofloxacin (99%, Sigma, US), Vancomycin hydrochloride (99%, Sigma, US), Potassium iodide (KI, 99%, Sigma, US), Isopropanol (99%, Aladdin, China), superoxide dismutase (SOD, 99%, Yuanye Bio, China).

2.2. Synthesis of CN with different crystallinity

Urea or thiourea is heated and cyclized to produce melamine. Melamine dimerizes to form honey white amines, which can be rearranged to form honey amines. When heated further, oligomers are formed flowed by CN [5,8]. This means that small-molecule precursors (e.g., urea, thiourea) exhibit higher entropy relative to melamine and have a more complex synthesis process in CN synthesis. At the same time, urea and thiourea as precursors release more gases during polymerization, and these gases also largely influence CN to become relatively disordered [28].

Inspired by this, the gas template method synthesized different crystallinity CN from the precursor. In a typical synthesis, melamine is dissolved in water and then sprayed onto the inside of a pre-heated crucible using an original spray device. After thoroughly drying, the loading capacity of melamine was 6.0 g and calcined at 550°C for 2 h with a heating ramp rate of $10^\circ\text{C min}^{-1}$. Then, slowly cooled to room temperature at the rate of 1°C min^{-1} . After the calcination process, to collect the formed yellow highly crystalline CN powder and wash it repeatedly with water to remove the unpolymerized melamine. Finally, the obtained High-crystallinity CN is fully freeze-dried. Besides, Medium-crystallinity CN and Low-crystallinity CN can be obtained by changing the precursor of melamine into thiourea and urea, respectively.

2.3. Synthesis of Tri-crystallinity CN

The melt-polymerization method was employed to synthesize Tri-crystallinity CN from the precursor. In a typical synthesis, 4.8 g urea, 0.4 g thiourea, and 0.8 g melamine were dispersed in 10 mL ethanol (that is, the ratio of raw materials is 12:1:2) and fully ground at 80°C for 10 min to make ethanol volatilize, and obtain a uniform mixture. First, the molten precursor is thoroughly mixed at 200°C for 2 h. They were later calcined at 600°C for 3 h with a heating ramp rate of $10^\circ\text{C min}^{-1}$. Then, slowly cooled to room temperature at the rate of 1°C min^{-1} . After the calcination process, the formed Tri-crystallinity CN powder was

collected.

2.4. Tri-crystallinity CN loaded on nonwoven fabrics

Tri-crystallinity CN loads on nonwoven fabrics to form flexible materials [29]. 100 mg Tri-crystallinity CN was dispersed in 200 mL deionized water and ultrasonic treatment for 10 min to obtain a uniform suspension. Spread evenly on clean and dry $100 \text{ cm} \times 100 \text{ cm}$ nonwoven fabric, further dry in a fume hood at room temperature. Repeat until all drops are applied to the nonwoven fabric.

2.5. Characterization

The morphologies were investigated with the field emission scanning electron microscopy (FE-SEM, Hitachi SU-8010), the transmission electron microscope (TEM, Hitachi HT-7700), the high-resolution transmission electron microscope (HR-TEM, JEOL JEM-2100 F) and the atomic force microscopy (AFM, SPM-9700). X-ray photoelectron spectroscopy (XPS) measurements were performed using an ESCALAB 250Xi instrument (Thermo Scientific) with Al K_α radiation. Single electrons captured by interface defects were detected using electron paramagnetic resonance (EPR) (Bruker EMXPlus). Raman spectrometer (HORIBA HR800) with the laser wavelength was at 633 nm were used. X-ray diffraction (XRD) is a Bruker D8 Advance X-ray diffractometer using a Cu $K\alpha 1$ ($\lambda = 1.5418 \text{ \AA}$) at 45 kV and 200 mA. The Fourier transform infrared (FT-IR) spectra were recorded on Bruker V70 spectrometer. UV-Vis diffuse reflectance spectroscopy (DRS) spectra were acquired through Hitachi U-3010 spectrophotometer with reference of BaSO_4 . Surface photovoltage (SPV) spectra were detected by a home-made instrument equipped with a lock-in amplifier (SR830, USA) synchronized with an optical chopper (SR540, USA). Monochromatic light resource was a 500 W xenon lamp (CHF XQ500W) with a double-prism monochromator (Omni- λ 3005). The photovoltage signal was amplified by a lock-in amplifier (SR830-DSP) with a light chopper (SR540). The resolution of spectrum was 1 nm. The raw surface photovoltage data were normalized using the illuminometer (Zolix UOM-1S). The steady-state photoluminescence (PL) spectra were measured on Edinburgh FS5 fluorescence spectrometer with an excitation wavelength of 351 nm.

2.6. Photocatalytic organic pollutants degradation test

The CN were used as catalysts for the degradation of model pollutant under full-spectrum. A 300 W Xe lamp was chosen as the light source. The comparison of photocatalyst activity was carried out in a batch reactor (Supporting Information 1.3 section). 10 mg of the photocatalyst was suspended in a 50 mL aqueous solution involving 10 mg L^{-1} pollutant, magnetically stirred under darkness for 30 min to achieve adsorption equilibrium.

During the photocatalytic degradation, collect 2 mL of the suspension at an interval of 1 min. They further centrifuged at 15000 rpm and measuring the pollutant concentration with a UV-3600 UV-VIS-NIR spectrophotometer (Shimadzu). In the cycle experiments, after completing the first catalytic experiment, all catalysts were collected and put into the subsequent catalytic investigation and repeated the process several times.

For active species trap experiments, the concentration of model pollutant was 10 mg L^{-1} superoxide dismutase (SOD, 0.4 g L^{-1}) and potassium iodide (KI, 10 mM) were used as effective scavengers of superoxide radical ($\cdot\text{O}_2^-$) and hole (h^+), respectively. Isopropyl alcohol (1.0 mM) was utilized as hydroxyl radical ($\cdot\text{OH}$) scavenger. Other conditions were consistent with the above photocatalytic experiments.

2.7. Continuous-flow photocatalytic organic wastewater degradation

Continuous-flow organic wastewater degradation experiments are carried out through our carefully designed large-scale photocatalytic

plate reactor (80 cm × 60 cm). The continuous flow reactor is made of polymethyl methacrylate and is equipped with a silver mirror at the bottom. The continuous-flow device comprises a water inlet system, photocatalytic reaction chambers, liquid detection system, and liquid collection system.

In detail, the inlet system consists of a mixing tank and a collection tank. The catch basin has a length × width × height = 60 cm × 11 cm × 5.5 cm. The photocatalytic reaction chamber consists of nine galleries with a uniform length of 60 cm, and a uniform height of 3 cm. The widths were 4, 5, 6, 6, 8, 8, 10, 10, and 10 cm, respectively. The photocatalyst Tri-crystallinity CN is supported on a nonwoven fabric and tiled into the reaction chamber. The effluent end is shunt to a mobile liquid phase UV detector (Sanotac, UV1001) and the rest to the water purification collection tank. The concentration of RhB was obtained from the absorbance of the UV detector at $\lambda = 556$ nm.

2.8. Photoelectrochemical measurements

Photoelectrochemical tests were performed on a CVB120 electrochemical workstation (Zahner, Germany) in a conventional three-electrode configuration. The working electrode prepared with the sample has an active area of ca. 1 cm². A Pt electrode and an Ag/AgCl electrode were used as the counter and reference electrode, respectively. A 300 W Xe lamp (Perfectlight PLS-SXE300) with a filter a light source

with the wavelength range of 320–780 nm was used as the light source.

Typically, the working electrodes were prepared as follows: 10 mg of photocatalyst sample was dissolved with mixture of 30 μ L ultrapure water. Then, the effective area of FTO glass was fixed to 1 cm² with insulating tape, and the dispersion solution was coated on the effective area. Finally, it was dried in the flowing air at 70 °C for 30 min

2.9. Calculation details

The density of electronic state and deformation charge density calculations were performed using density functional theory (DFT), as implemented in the Dmol3 program based on Materials Studio 8.0. The generalized gradient approximation (GGA) method described electronic exchange correlation energy with Perdew-Burke-Ernzerhof (PBE) functional. The double numerical plus polarization (DNP) basis defined valence orbitals. We obtained the geometry optimization and characterization of the electronic structure from the M062X/def2-TZVP [14] and the reaction energy profile from the b3lyp/def2-TZVP calculations [15].

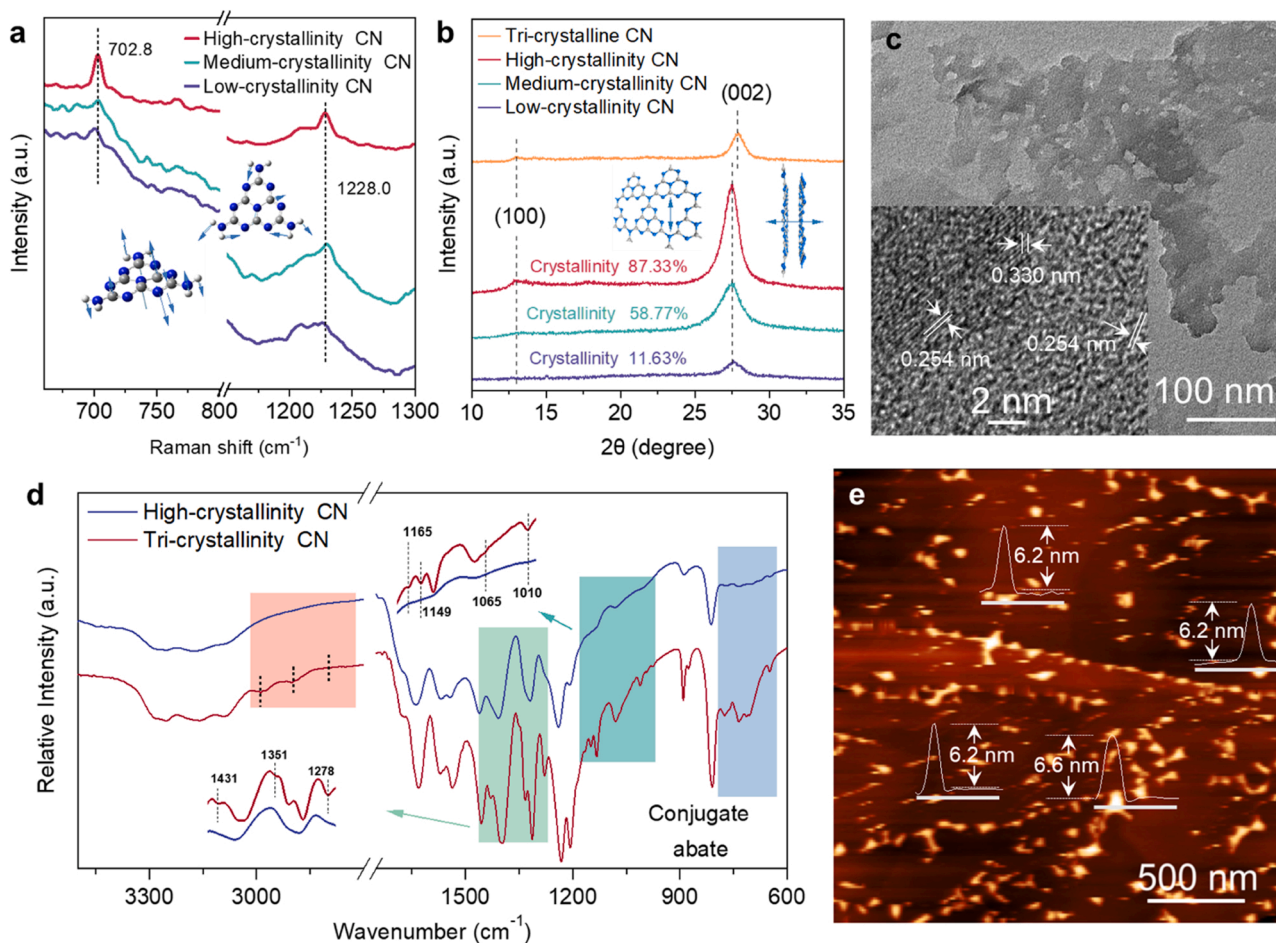


Fig. 1. Construction of Tri-crystallinity CN homojunction. (a) Raman spectra. Inset: frequencies of the heptazine ring calculated by DFT (b3lyp 6–311 +G* level), with arrows indicating the direction and amplitude of the Raman vibration. Corresponding to the peaks located at 702.8 and 1228.0 cm^{−1} in the Raman spectrum, respectively. (b) XRD patterns of CN with various crystallinity. Inset: The structure on the left represents the in-plane period of the heptazine ring unit, and the right shows the interlayer period. The length of the arrow represents a repeating unit. They refer to the (100) and (002) crystal planes in XRD, respectively. (c) HR-TEM image of Tri-crystallinity CN. (d) FT-IR spectroscopy of High-crystallinity CN and Tri-crystallinity CN. (e) Atomic Force Microscope (AFM) image of Tri-crystallinity CN.

3. Results and discussion

3.1. Preparation of Tri-crystallinity CN homojunction

We employed the gas template method to synthesize CN Homo-junction with Tri-crystallinity. The regulatory mechanism was derived from the template heat treatment of S-, O-, and N- produced during polymerization. Due to the template effect of gas generated at the polymerization process, we can precisely regulate the conjugation degree of the product by controlling the template gas and temperature under carefully designed polymerization conditions [24]. High-crystallinity CN, Medium-crystallinity CN, and Low-crystallinity CN were prepared as comparisons to demonstrate the structure of the Tri-crystallinity CN (Figs. S1–S2). The N/C ratio was confirmed by the STEM-EDS elemental mapping analysis (Figs. S3–S6), where the distribution of N and C is high through the analyzed area.

Through elemental analysis, no S atom was detected in the product of thiourea polymerization (Fig. S7), which excludes the influence of the elements doped on the different CNs. Higher Raman signals are indicative of higher crystallinity [30]. Correspondingly, High-crystallinity CN presents a sharp Raman peak, confirming the existence of a high crystallinity structure (Fig. 1a). The inset in Fig. 1a exhibits the orientation and amplitude of the Raman peaks at 702.8 and 1228.0 cm^{-1} in the heptazine ring. With the decrease of crystallinity, the intensity of the peak decreases gradually. In X-ray diffraction (XRD) patterns (Fig. 1b), two diffraction peaks located at $\sim 13.1^\circ$ and $\sim 27.3^\circ$ correspond to (100) repeating structures in a two-dimensional plane and (002) interlayer stacking in CN [31]. The intensity of CN diffraction peak with three crystallinity is significantly different, and the fitting crystallinity is 87.33%, 58.77%, and 11.63%, respectively [32] (Table S1). Raman and XRD results suggest that the gas template method can successfully regulate the crystallinity of CN. For Tri-crystallinity, the (002) peak has a positive deviation of 0.5° over the pure High-crystallinity CN, attributed to the decrease in interlayer distance and the difference in planar crystallinity. It is proved that the structure of the interlayer interface of homojunction CN has changed.

High-resolution TEM (HR-TEM) analysis gives direct evidence for the CN with different crystallinity and the formation of Tri-crystallinity CN. The lattice fringe spacing is 0.254 nm and 0.330 nm, which correspond to the planar heptazine ring structure and interlaminar stacking of CN, respectively [25] (Fig. 1c). The obvious crystal difference in the nano-region predicts the coexistence of heptazine polymers with different crystallinity on Homojunction CN. In addition, the thermal decomposition temperature of the Tri-crystallinity CN was significantly enhanced compared to that of the single-phase CN (Fig. S8), attributed to the formation of interfaces that elevated the thermal decomposition temperature [33]. This again demonstrates the presence of CN with different crystallinity in the Tri-crystallinity CN.

FT-IR spectra give further evidence of a Tri-crystallinity structure (Fig. 1d). A similar tendency between Tri-crystallinity CN and High-crystallinity CN suggest the retained heptazine-based form. Apart from those maintained absorption peaks (strengthened or weakened), several new bands arose, ascribing to the deformation vibrations of the regular arrangement of molecular chains. This feature indicates the diversity of crystallinity. In detail, the band located around 750 cm^{-1} corresponds to the out-of-plane bending modes of C-N hetero-cycles shows an apparent increase, attributing to the abate of the conjugate of crystallinity in Tri-crystallinity CN. The cleavage zone between 1010 \sim 1165 cm^{-1} and 1278 \sim 1431 cm^{-1} indicates that the internal tension/strain and orientation are enhanced [26], implying the changes in the crystal domain. The absorption band near 2800 cm^{-1} is a symmetric and asymmetric stretch caused by changes in the C-H crystal domain. This may mean that different crystallinity CN exists. The Atomic Force Microscope (AFM) results showed the characteristics of nanofragment-like nanosheets of Tri-crystallinity CN with an average thickness of about 6.5 nm (Fig. 1e). Different crystallinity of CN forms abundant contact

interfaces within the homojunction CN.

3.2. Enhancing the interfacial IEF by the different crystallinity of CN

Differences in crystallinity produce changes in Fermi levels and energy band positions, enabling band bending in the space charge region and at interfaces. We infer that the interfacial IEF would exist in Tri-crystallinity CN by rationally constructing multiple interfaces [34,35]. Firstly, the effect of crystallinity on the CN front line orbital position was predicted based on density functional theory (DFT) simulations (Fig. S9). The *p*-orbital analysis of localized orbital locator (LOL) intuitively shows the conjugation of Heptazine-based polymers with different flatness [36]. The melen trimers with higher conjugation have slightly lower HOMO and LUMO levels (-7.779 and -1.593 eV, respectively) than lower conjugation (for HOMO and LUMO, -7.438 and -0.561 eV, respectively). Further, we predicted the work function is 5.16, 5.20, and 5.24 eV for Low-crystallinity, Medium-crystallinity, and High-crystallinity CN, respectively (Fig. 2a). The experimentally tested energy band positions (Fig. S10–S11) further confirm the trend of the energy band positions of CNs with crystallinity differences, as shown in Fig. 2b.

This feature allows interfacial IEF established between CNs with different crystallinity. As shown in Fig. 2c, when different crystallinity CN come in contact to form an interface, electrons flow from CN with higher Fermi level positions to lower [37]. Meanwhile, holes flow opposite to the electrons until the Fermi levels are equal. As the above thermal equilibrium state proceeds, space charge regions are formed on both sides of the interface. The higher crystallinity CN is a negative space charge region, and the lower is a positive space charge region. Thus, an interfacial IEF is formed from the lower crystallinity to the higher. Under illumination, the IEF drives photogenerated holes to migrate to the higher crystallinity CN and photogenerated electrons to the lower crystallinity CN. Combined with the energy band bending feature at the interface, the Tri-crystallinity CN would form a Z-scheme [38].

Having already understood the origin of interfacial IEF, we then explored the evidence for the existence of IEF. Since differential charge density demonstrates the accumulation of electrons and holes at the interface after photoexcitation, we use differential electron density analysis to describe interfacial IEF in Tri-crystallinity CN. As shown in Fig. 3a, at the High/Medium-crystallinity interface, the High-crystallinity CN exhibits the accumulation of photogenerated holes after photoexcitation. Similarly, at the Medium/Low-crystallinity interface, photogenerated holes accumulate at the Medium-crystallinity CN (Fig. 3b). This photogenerated charge accumulation feature confirms the presence and direction of IEF.

Besides theoretical calculations, experimental results further characterize the IEF. The Poisson equation describes the spatial distribution of the electric field of IEF (Fig. S12–S13), which shows that IEF is a function of surface potential and surface charge density [39–41]. Compared with the a conventional single-interface, the Tri-crystallinity has an enhanced IEF. According to the normalization of the calculated results, the value of Tri-crystallinity is about two times higher than that of a conventional single-interface (Fig. 3c, and Table S2). In addition, the IEF expressed as a log *I*-*V* curve based on cyclic voltammetry test shows the same trend (Fig. S14)[42]. This indicates that the multiple IEF can play a synergistic role and accelerate the charge transfer process [43].

The electrochemical impedance spectroscopy (EIS) reflects the migration efficiency of the photogenerated carriers. The charge transfer process of the working electrode is monitored using an equivalent circuit as shown in the inset of Fig. 3d to simulate the electrochemical process of the working electrode. The Tri-crystallinity CN exhibits a much-decreased charge transfer resistance ($R_{ct}=2.52$ k Ω). In comparison, the value for High-crystallinity CN, Medium-crystallinity CN, Low-crystallinity CN, and High /Low-crystallinity CN is 149.49 k Ω ,

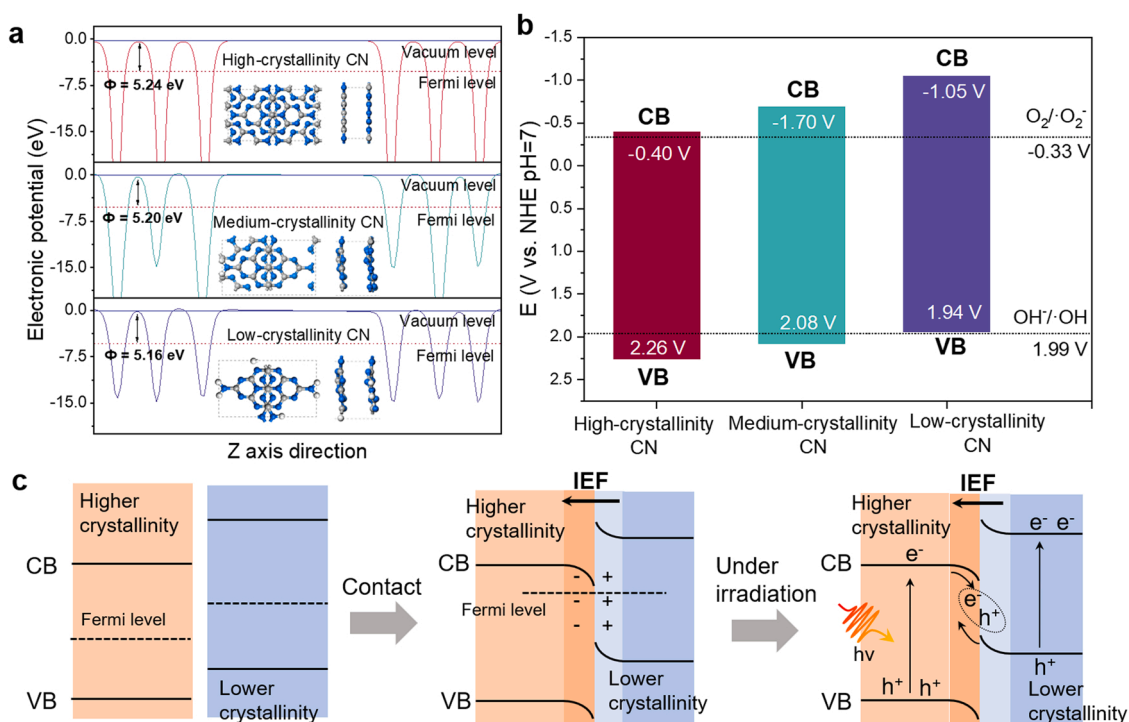


Fig. 2. Crystallinity difference enhances the interfacial IEF of Homojunction CN. (a) Spatial distribution of electron potential energy and Fermi level position, (b) band positions of High-crystallinity CN, Medium-crystallinity CN, and Low-crystallinity CN. (c) Interfacial IEF formation and the driving effect on photogenerated carriers for Homojunction CN. Schematic diagram of interfacial IEF generation and the driving effect on photogenerated carriers for Homojunction CN.

126.05 k Ω , 13.69 k Ω and 3.78 k Ω , respectively. In contrast, Tri-crystallinity CN processes the lowest charge transfer resistance, attributing to the driving effect of the interfacial IEF.

3.3. Boosting charge-carrier separation by Tri-crystallinity CN

The multiplex interfacial IEF in Tri-crystallinity CN drives photo-generated carrier migration, enabling reduced recombination of photogenerated electron-hole pairs. This was demonstrated by the steady-state photoluminescence (PL) spectra (Fig. 4a). Tri-crystallinity CN shows a quenching emission relative to pure High-crystallinity CN, indicating the intrinsic radiative recombination of photogenerated electron-hole pairs has been substantially inhibited. This feature suggests that the interfacial IEF in Homojunction CN efficiently drives charge migration, resulting in weak charge recombination. Moreover, the transient PL spectra display that the Homojunction CN possesses a longer average lifetime (τ_A) of charge carriers (Fig. 4b), exhibiting the efficient charge-carrier separation in the multiple interfaces. The increase in carrier lifetime τ_A enhances the possibility of their participation in photocatalytic reactions before recombination [44,45].

The separated photogenerated charges have an opportunity to migrate to the surface of the photocatalyst. Tri-crystallinity CN exhibits a much higher photocurrent response than other samples as-prepared, confirming abundant charges separated (Fig. 4c). In addition, the photocurrent did not decrease during the 500 s test, suggesting the stability of Tri-crystallinity CN. The surface photovoltage (SPV) directly reflects the state of accumulation of photogenerated charges on the surface. All the SPV responses show positive signals in the 300–450 nm (Fig. 4d). This indicates that, the photogenerated holes transfer to the surface of the semiconductor under illumination in the range of 300–450 nm, showing the characteristics of an N-type semiconductor [46]. Notably, the Tri-crystallinity CN possesses an SPV signal of up to 11 μ V, pointing to plenty of photogenerated charge reaching to the surface.

The charge separation process derived by IEF is explored from the

point of view of charge carrier dynamics. Charge-carriers separation and capture processes in CN are detected by femtosecond transient absorption spectroscopy (fs-TAS). The excited-state absorption peaks for 700–1300 nm are assigned to trapped and shallowly trapped photo-generated electrons. Then, the time profiles of fs-TAS probed at 1150 nm were also fitted to estimate the decay kinetics of photogenerated carriers. Compared with High/Low-crystallinity CN (Fig. 4e), the lifetime (τ_1) of the captured electrons in the Tri-crystallinity CN is significantly reduced to 15.44 ps, indicating that enhanced IEF by multiple interfaces achieves faster charge-carrier separation. Simultaneously, the τ_2 and τ_3 referring to the excited electrons relaxation process exhibit significantly increased delay, owing to the interfacial IEF inhibited recombination (Fig. 4f).

Based on the above results, we verify that the interfacial IEF established at multiple crystallinity difference interfaces is favorable for charge-carrier separation. Thus, efficient photocatalytic degradation is expected in surface catalytic reactions.

3.4. Boosting photocatalytic degradation of pollutants by Tri-crystallinity CN

A strictly designed parallel multi-channel batch reactor tested the photocatalytic degradation of different CN photocatalysts. Excluding the effect of total photon absorption rate (Fig. S15–S19) [47–49], we attribute the difference in photocatalytic activity to the impact of photogenic charge behavior. The exceptional charge separation properties derived from interfacial IEF confer excellent photocatalytic degradation performance of Tri-crystallinity CN under visible light. RhB was used as a model pollutant to study the photocatalytic degradation kinetics of CN. Compared with the pure CN, the homojunction CN exhibited superior photocatalytic activity due to the acceleration of charge-carrier separation (Fig. S20–S22 & Fig. 5a). In particular, the rate of RhB photo-degradation with Tri-crystallinity CN (0.673 min $^{-1}$) is 56.08 times higher than High-crystallinity CN (0.012 min $^{-1}$). We combined two or three CNs in a physical mixture to highlight the importance of interface

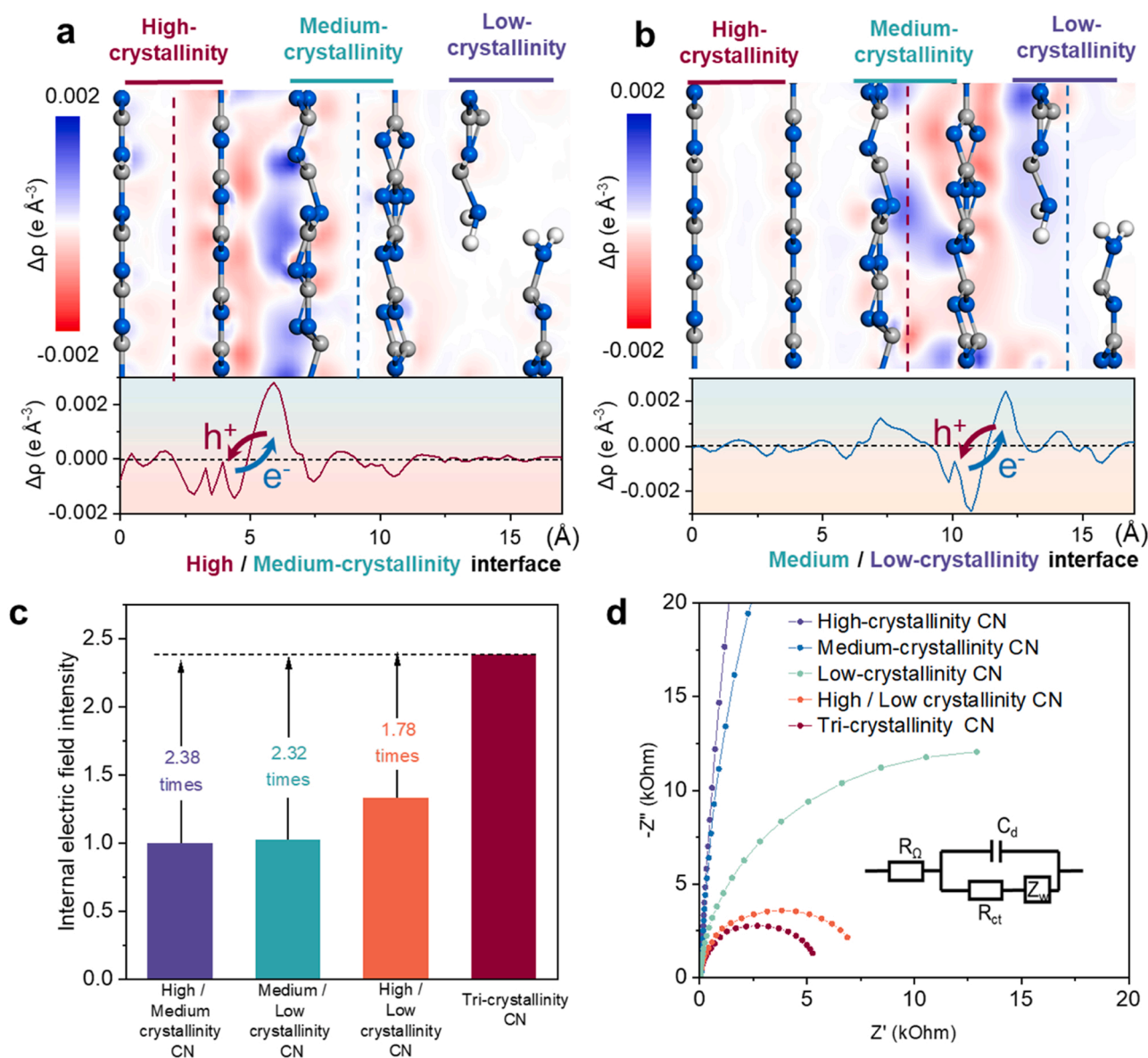


Fig. 3. The interfacial IEF in Tri-crystallinity CN facilitates the separation of photogenerated carriers. Section of the average electron density deformation side view $\Delta\rho(z)$ and deformation charge density at (a) High/Medium-crystallinity interface and (b) Medium/Low-crystallinity interface. The red and blue areas indicate electron depletion and accumulation, respectively. The gray, blue, and white spheres respectively denote C, N, and H atoms. (c) Experimental characterization of the IEF intensity of different homojunction CN. (d) Electrochemical impedance spectra (EIS) of pure CN and homojunction CN. Where R_{Ω} , C_d , R_{ct} , Z_w are solution resistance, double layer capacitance at the research electrode interface, charge transfer resistance, Warburg impedance respectively.

formation for photocatalytic activity. Ignoring the yield effect, we formulated the physically mixed CN according to the ratio of raw materials used to prepare Tri-crystallinity CN (Low-crystallinity: Medium-crystallinity: High-crystallinity = 12:1:2). No activity increase was observed in the mixture, suggesting that the formation of the crystallinity difference interface is essential.

Moreover, such efficient photocatalytic degradation is also widely applicable to other aromatic antibiotic pollutants. The degradation rate of levofloxacin, tetracycline, ciprofloxacin and vancomycin by Tri-crystallinity CN was 429, 29, 72, and 56 times higher than that of High-crystallinity CN (Fig. 5b). Tri-crystallinity CN has demonstrated favorable stability in cyclic degradation of RhB and has potential for large-scale application (Fig. 5c). In addition, Tri-crystallinity CN also showed efficient removal of pollutants under natural sunlight (Fig. S23). XRD and FT-IR exhibited no increasing or decreasing peaks (Fig. S24), indicating the stability of the Tri-crystallinity CN (Fig. S23).

To identify active species produced during photodegradation,

superoxide dismutase (SOD), potassium iodide (KI), and isopropyl alcohol were employed as a scavenger for superoxide radical ($\cdot\text{O}_2^-$), hole (h^+), and hydroxyl radical ($\cdot\text{OH}$), respectively [50,51]. Fig. 5d shows that KI significantly inhibits the degradation of RhB. Meanwhile, SOD and isopropanol also decrease the degradation process. Thus, the synergistic effect of $\cdot\text{O}_2^-$, h^+ , and $\cdot\text{OH}$ promotes the degradation of RhB. Moreover, we excluded the contribution of singlet oxygen to the photocatalytic degradation reaction (Fig. S25). We applied electron paramagnetic resonance (EPR) analysis to verify the generated active species. 5, 5-dimethyl-1-pyrroline-N-oxide (DMPO) was used as a collector to detect $\cdot\text{O}_2^-$ and $\cdot\text{OH}$ in methanol and water, respectively. As shown in Fig. 5e, a six-fold signal derived from DMPO- $\cdot\text{O}_2^-$ adduct was detected in Homojunction CN. Furthermore, we also noticed the 1: 2: 2: 1 characteristic peak of DMPO- $\cdot\text{OH}$ adduct (Fig. 5f). The significant difference in the intensities of Tri-crystallinity CN and pure High-crystallinity CN demonstrates that Tri-crystallinity CN enhances $\cdot\text{O}_2^-$ and $\cdot\text{OH}$ production. The above results verify the essential

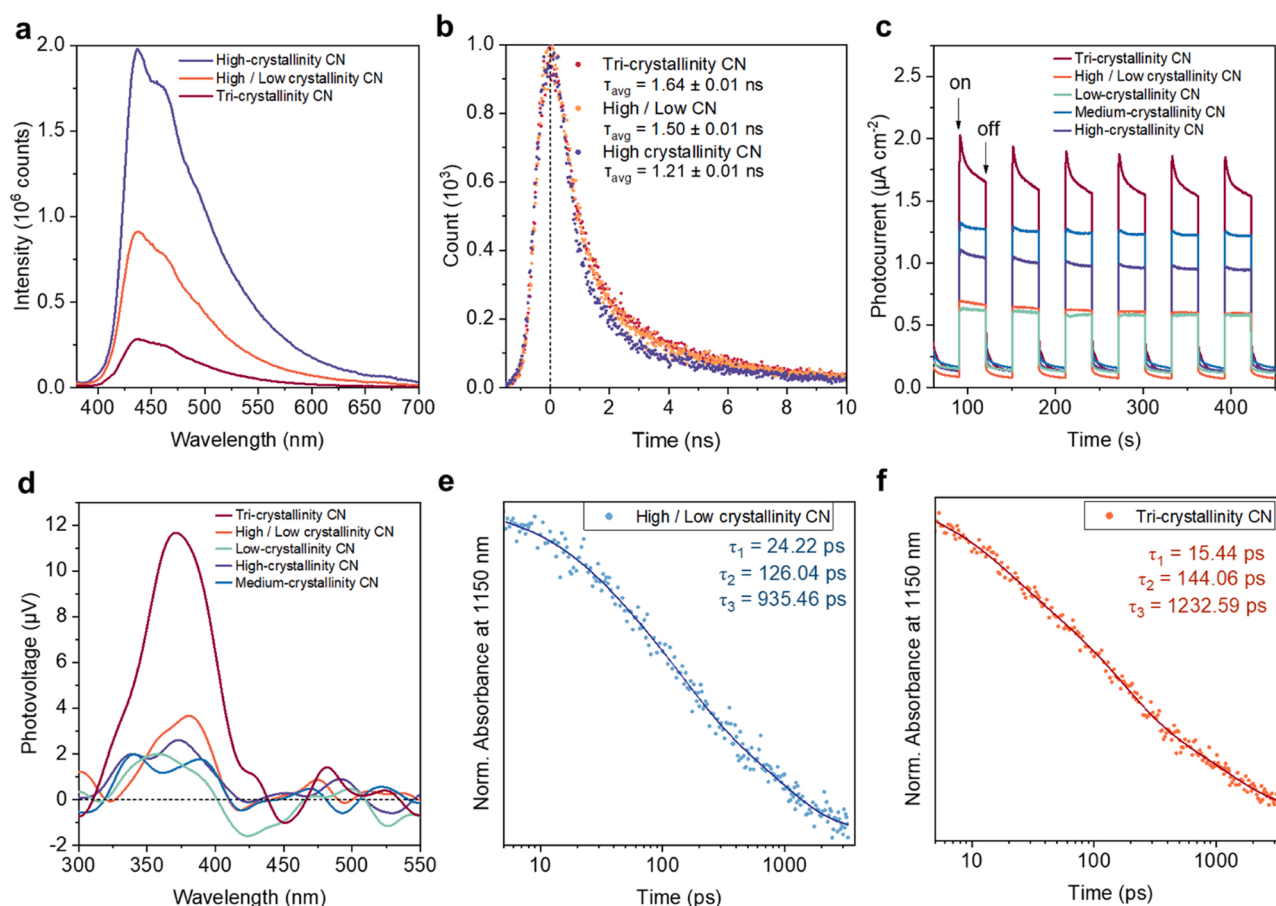


Fig. 4. The enhanced interfacial IEF promotes photogenerated charge-carrier separation. (a) Steady-state photoluminescence spectra. (b) Time-resolved photoluminescence kinetics monitoring at 450 nm. (c) Transient photocurrent response. (d) surface photovoltage (SPV) spectrum. Femtosecond transient absorption spectrum of (e) High-crystallinity/Low-crystallinity CN and (f) Tri-crystallinity CN.

role of the interfacial IEF in the charge-carrier separation and the reactive oxygen species generation, which endowed Tri-crystallinity CN with outstanding photocatalytic degradation activity among similar materials (Table S3).

For the Tri-crystallinity CN with the best photocatalytic performance, we demonstrated the purification effect in a continuous flow reactor to exhibit the prospect of industrial application. The dispersion of photocatalysis powders in wastewater is challenging to implement in a continuous-flow reactor because of the high separation cost. This poses a challenge to the rational design of the photocatalytic reactor. We designed an 80 cm × 60 cm continuous-flow reactor composed of four parts (Fig. 6a). They are a water inlet system, photocatalytic reaction chambers, liquid detection system, and liquid collection system (Experimental section). To improve the light absorption efficiency of the overall fabric device, increasing the light absorption on the backside is an effective way to enhance the photocatalytic degradation. We placed a silver mirror at the bottom of the flow channel to reflect the photons projected to the backside (Fig. S28-S29), thus activating the photocatalyst on the original backside.

High concentrations of pollutants and tap water are pumped through peristaltic pumps into the mixing tank to mix well in the water inlet system. The initial concentration of organic pollutants is regulated by controlling the peristaltic pump. The effluent flows into a catchment tank to stabilize the water. It then flows into the nine photocatalytic reaction chambers through an overflow weir with oxygen aeration function. The bottom of each flow channel layer is covered with a nonwoven fabric substrate that firmly supports Tri-crystallinity CN (Fig. 6b). The water flow zigzags along the flow channel at an angle of

180° to obtain a longer residence time and enhanced mass transfer efficiency between catalyst and liquid. In particular, a liquid detection system is integrated into the last flow channel to detect the quality of the purified wastewater in real-time through an absorption spectrum detector. Finally, all wastewater is fed into the liquid collection system through the diversion tank to obtain purified water.

To evaluate the operation effect of the device more intuitively, RhB is used as a visual model of organic pollutants for evaluation (Fig. 6c). The continuous flow reactor unit operates in outdoor sunlight and the experiments were carried out at solar irradiation to the continuous flow reactor at an intensity of about 80 mW/cm² (Fig. S30). At a flow rate of 14.2 L h⁻¹ m⁻², the removal rate of RhB was maintained above 91.0% under outdoor sunlight from 11:00 a.m. to 3:00 p.m. (Fig. 6d). When running at a higher flow rate (20.83 L h⁻¹ m⁻²), the device's removal rate of RhB in wastewater was maintained at 90.0%, and it could remove up to 17.45 mg of RhB per square meter per hour (Fig. 6e). Even after a long period of operation (10 h), the removal rate remained stable (Fig. S31). Thus, the supported photocatalytic system based on Tri-CN has a vital application prospect in wastewater degradation under actual environmental conditions.

4. Conclusions

In conclusion, we present a homojunction CN photocatalyst that enhances interfacial IEF through crystallinity difference. The degradation activity for various antibiotics of Tri-crystallinity CN is at least 20 times greater than that of pure High-crystallinity CN. And the photocatalyst loading on a nonwoven fabric in a continuous-flow reactor to

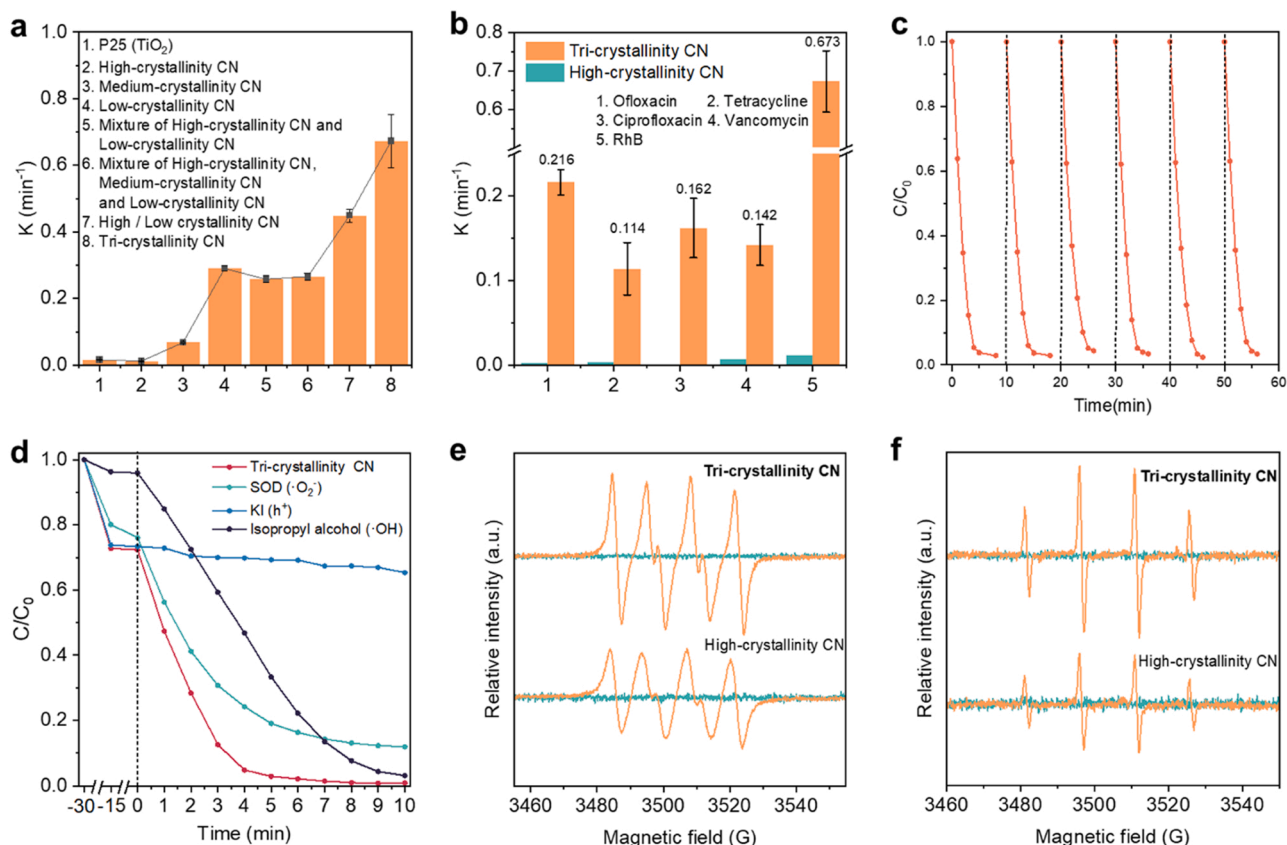


Fig. 5. The interfacial IEF of Tri-crystallinity CN promotes photocatalytic degradation of pollutants. (a) Different degradation rate towards RhB among samples prepared. $c_{\text{cat.}} = 0.2 \text{ g L}^{-1}$, $c_{\text{RhB}} = 0.01 \text{ g L}^{-1}$, photocatalytic reaction time = 10 min, pH = 8.1. (b) Different degradation rate towards Ofloxacin, Tetracycline, Ciprofloxacin, Vancomycin, and RhB. (c) The cycle stability experiment of Tri-crystallinity CN for the RhB degradation. (d) Effect of quenching agent on the degradation of RhB by Tri-crystallinity CN. EPR spectrum for the detection of (e) $\text{O}_2^{\cdot-}$ and (f) $\cdot\text{OH}$ in the presence of 5,5-dimethyl-1-pyrroline-N-oxide (DMPO).

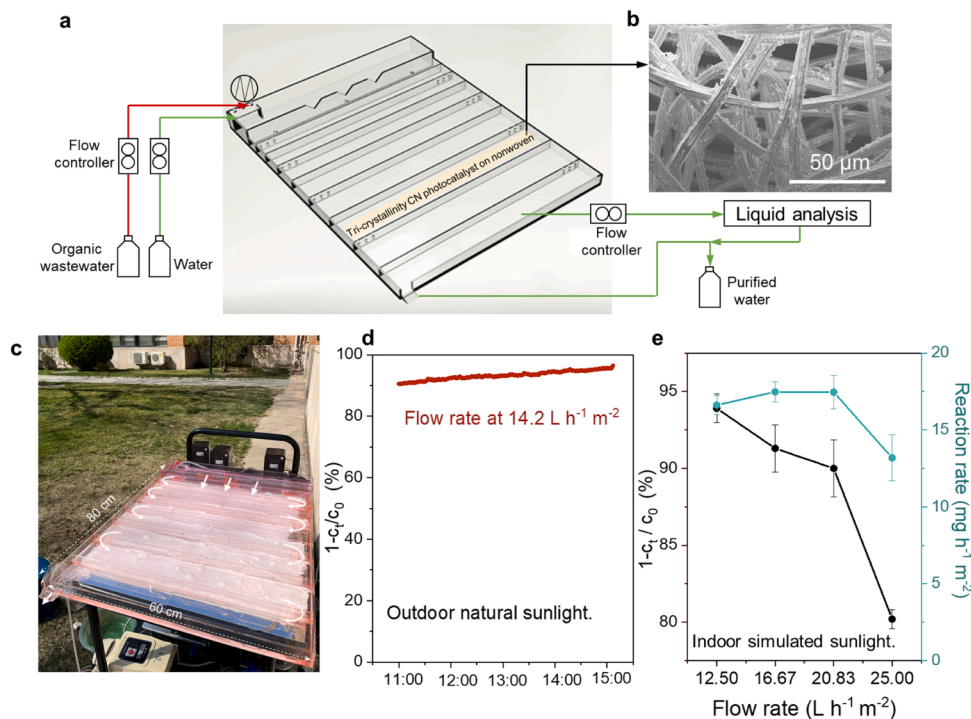


Fig. 6. Efficient degradation pollutants for Tri-crystallinity CN in continuous-flow reactor. (a) Schematic diagram of continuous-flow reactor for photocatalytic degradation pollutants. (b) SEM image of nonwoven fibers loaded with Tri-crystallinity CN. (c) Photograph of photocatalytic degradation of RhB by Tri-crystallinity CN in a continuous flow device. Arrows indicate the direction of water flow. (d) Photocatalytic degradation RhB by outdoor sunlight at outdoor natural sunlight. The irradiation intensity to the continuous flow reactor is about 80 mW cm^{-2} . (e) Residual rate and photocatalytic reaction rate of RhB in continuous-flow reactor at indoor simulated sunlight. $c_{\text{cat.}} = 0.021 \text{ mg cm}^{-2}$, pH = 8.1.

achieve more than 91.0% degradation at a high flow rate of $14.2 \text{ L h}^{-1} \text{ m}^{-2}$ from 11:00 a.m. to 3:00 p.m. under outdoor sunlight. By rationally designing interfacial IEF via the crystallinity difference, this work has developed a homogeneous structural construction scheme with wide adaptability, gaining valuable prospects for industrial applications of photodegradation.

CRediT authorship contribution statement

Yan Guo: Writing – review & editing, Conceptualization, Methodology, Software. **Sijie Huang:** Investigation, Data curation. **Yang Guo:** Resources, Visualization, Investigation. **Zhiqiang Ye:** Validation, Resources. **Jun Nan:** Resources, Conceptualization. **Qixin Zhou:** Software, Writing – original draft, Project administration. **Yongfa Zhu:** Supervision, Funding acquisition.

Declaration of Competing Interest

The authors declare that they have no known competing financial interests or personal relationships that could have appeared to influence the work reported in this paper.

Acknowledgements

This work was supported by National Science Foundation of China (21872077), National Key Research and Development Project of China (2020YFA0710304), and Collaborative Innovation Center for Regional Environmental Quality.

Appendix A. Supporting information

Supplementary data associated with this article can be found in the online version at [doi:10.1016/j.apcatb.2022.121388](https://doi.org/10.1016/j.apcatb.2022.121388).

References

- [1] P.M.C. Huijbers, H. Blaak, M.C.M. De Jong, E.A.M. Graat, C.M.J.E. Vandenbroucke-Grauls, A.M. De Roda Husman, Role of the environment in the transmission of antimicrobial resistance to humans: a review, *Environ. Sci. Technol.* 49 (2015) 11993–12004.
- [2] B.M. Marshall, S.B. Levy, Food animals and antimicrobials: impacts on human health, *Clin. Microbiol. Rev.* 24 (2011) 718–733.
- [3] D. Kong, B. Liang, H. Yun, H. Cheng, J. Ma, M. Cui, A. Wang, N. Ren, Cathodic degradation of antibiotics: characterization and pathway analysis, *Water Res.* 72 (2015) 281–292.
- [4] A.C. Singer, H. Shaw, V. Rhodes, A. Hart, Review of antimicrobial resistance in the environment and its relevance to environmental regulators, *Front. Microbiol.* 7 (2016).
- [5] W.-J. Ong, L.-L. Tan, Y.H. Ng, S.-T. Yong, S.-P. Chai, Graphitic carbon nitride (g-C₃N₄)-based photocatalysts for artificial photosynthesis and environmental remediation: are we a step closer to achieving sustainability? *Chem. Rev.* 116 (2016) 7159–7329.
- [6] Y. Guo, W. Shi, Y. Zhu, Y. Xu, F. Cui, Enhanced photoactivity and oxidizing ability simultaneously via internal electric field and valence band position by crystal structure of bismuth oxyiodide, *Appl. Catal. B: Environ.* 262 (2020), 118262.
- [7] P. Chen, L. Blaney, G. Cagnetta, J. Huang, B. Wang, Y. Wang, S. Deng, G. Yu, Degradation of ofloxacin by perylene diimide supramolecular nanofiber sunlight-driven photocatalysis, *Environ. Sci. Technol.* 53 (2019) 1564–1575.
- [8] F.K. Kessler, Y. Zheng, D. Schwarz, C. Merschjann, W. Schnick, X. Wang, M. J. Bojdys, Functional carbon nitride materials — design strategies for electrochemical devices, *Nat. Rev. Mater.* 2 (2017) 17030.
- [9] M. Jourshabani, B.-K. Lee, Z. Shariatnia, From traditional strategies to z-scheme configuration in graphitic carbon nitride photocatalysts: recent progress and future challenges, *Appl. Catal. B-Environ.* 276 (2020), 119157.
- [10] Y. Guo, W. Shi, Y. Zhu, Electric field engineering for steering photogenerated charge separation and enhancing photoactivity, *EcoMat* 2 (2019) 12007.
- [11] J. Li, L. Cai, J. Shang, Y. Yu, L. Zhang, Giant enhancement of internal electric field boosting bulk charge separation for photocatalysis, *Adv. Mater.* 28 (2016) 4059–4064.
- [12] X. Zhang, F. Tian, M. Gao, W. Yang, Y. Yu, L-Cysteine capped Mo₂C/ZnO₆₇Cd_{0.33}S heterojunction with intimate covalent bonds enables efficient and stable H₂-Releasing photocatalysis, *Chem. Eng. J.* 428 (2022), 132628.
- [13] Y. Yu, W. Yan, X. Wang, P. Li, W. Gao, H. Zou, S. Wu, K. Ding, Surface engineering for extremely enhanced charge separation and photocatalytic hydrogen evolution on g-C₃N₄, *Adv. Mater.* 30 (2018).
- [14] H. Huang, S. Tu, C. Zeng, T. Zhang, A.H. Reshak, Y. Zhang, Macroscopic polarization enhancement promoting photo- and piezoelectric-induced charge separation and molecular oxygen activation, *Angew. Chem. Int. Ed. Engl.* 56 (2017) 11860–11864.
- [15] L. Hao, L. Kang, H. Huang, L. Ye, K. Han, S. Yang, H. Yu, M. Batmunkh, Y. Zhang, T. Ma, Surface-halogenation-induced atomic-site activation and local charge separation for superb CO₂ photoreduction, *Adv. Mater.* 31 (2019), e1900546.
- [16] Z. Lin, X. Wang, Nanostructure engineering and doping of conjugated carbon nitride semiconductors for hydrogen photosynthesis, *Angew. Chem. Int. Ed.* 52 (2013) 1735–1738.
- [17] G. Zhang, M. Zhang, X. Ye, X. Qiu, S. Lin, X. Wang, Iodine modified carbon nitride semiconductors as visible light photocatalysts for hydrogen evolution, *Adv. Mater.* 26 (2014) 805–809.
- [18] Z. Ding, X. Chen, M. Antonietti, X. Wang, Synthesis of transition metal-modified carbon nitride polymers for selective hydrocarbon oxidation, *ChemSusChem* 4 (2011) 274–281.
- [19] J. Ran, T.Y. Ma, G. Gao, X.-W. Du, S.Z. Qiao, Porous P-doped graphitic carbon nitride nanosheets for synergistically enhanced visible-light photocatalytic H₂ production, *Energy Environ. Sci.* 8 (2015) 3708–3717.
- [20] J. Zhang, G. Zhang, X. Chen, S. Lin, L. Möhlmann, G. Dolega, G. Lipner, M. Antonietti, S. Blechert, X. Wang, Co-monomer control of carbon nitride semiconductors to optimize hydrogen evolution with visible light, *Angew. Chem. Int. Ed.* 51 (2012) 3183–3187.
- [21] J. Zhang, X. Chen, K. Takanabe, K. Maeda, K. Domen, J.D. Epping, X. Fu, M. Antonietti, X. Wang, Synthesis of a carbon nitride structure for visible-light catalysis by copolymerization, *Angew. Chem. Int. Ed.* 49 (2010) 441–444.
- [22] Z. Zhang, Y. Zhu, X. Chen, H. Zhang, J. Wang, A full-spectrum metal-free porphyrin supramolecular photocatalyst for dual functions of highly efficient hydrogen and oxygen evolution, *Adv. Mater.* 31 (2019), e1806626.
- [23] P. Ma, X. Zhang, C. Wang, Z. Wang, K. Wang, Y. Feng, J. Wang, Y. Zhai, J. Deng, L. Wang, K. Zheng, Band alignment of homojunction by anchoring CN quantum dots on g-C₃N₄ (0D/2D) enhance photocatalytic hydrogen peroxide evolution, *Appl. Catal. B: Environ.* 300 (2022), 120736.
- [24] G. Ba, Z. Liang, H. Li, N. Du, J. Liu, W. Hou, Simultaneous formation of mesopores and homojunctions in graphite carbon nitride with enhanced optical absorption, charge separation and photocatalytic hydrogen evolution, *Appl. Catal. B-Environ.* 253 (2019) 359–368.
- [25] H. Wang, X. Sun, D. Li, X. Zhang, S. Chen, W. Shao, Y. Tian, Y. Xie, Boosting hot-electron generation: exciton dissociation at the order-disorder interfaces in polymeric photocatalysts, *J. Am. Chem. Soc.* 139 (2017) 2468–2473.
- [26] S. Sun, J. Li, P. Song, J. Cui, Q. Yang, X. Zheng, Z. Yang, S. Liang, Facile constructing of isotype g-C₃N₄(bulk)/g-C₃N₄(nanosheet) heterojunctions through thermal polymerization of single-source glucose-modified melamine: an efficient charge separation system for photocatalytic hydrogen production, *Appl. Surf. Sci.* 500 (2020), 143985.
- [27] H. Dong, X. Zhang, J. Li, P. Zhou, S. Yu, N. Song, C. Liu, G. Che, C. Li, Construction of morphology-controlled nonmetal 2D/3D homojunction towards enhancing photocatalytic activity and mechanism insight, *Appl. Catal. B-Environ.* 263 (2020), 118270.
- [28] G. Li, Z. Xie, S. Chai, X. Chen, X. Wang, A facile one-step fabrication of holey carbon nitride nanosheets for visible-light-driven hydrogen evolution, *Appl. Catal. B-Environ.* 283 (2021), 119637.
- [29] K. Ma, P. Li, J.H. Xin, Y. Chen, Z. Chen, S. Goswami, X. Liu, S. Kato, H. Chen, X. Zhang, J. Bai, M.C. Wasson, R.R. Maldonado, R.Q. Snurr, O.K. Farha, Ultrastable mesoporous hydrogen-bonded organic framework-based fiber composites toward mustard gas detoxification, *Cell Rep. Phys. Sci.* 1 (2020), 100024.
- [30] Z. Zafar, A. Zafar, X. Guo, Q. Lin, Y. Yu, Raman evolution of order-disorder phase transition in multiaxial molecular ferroelectric thin film, *J. Raman. Spectrosc.* 50 (2019) 1576–1583.
- [31] X. Chen, R. Shi, Q. Chen, Z. Zhang, W. Jiang, Y. Zhu, T. Zhang, Three-dimensional porous g-C₃N₄ for highly efficient photocatalytic overall water splitting, *Nano Energy* 59 (2019) 644–650.
- [32] L. Alexander, X-ray diffraction methods in polymer science, *J. Mater. Sci.* 6 (1971), 93–93.
- [33] J. Li, G. Zhan, Y. Yu, L. Zhang, Superior visible light hydrogen evolution of Janus bilayer junctions via atomic-level charge flow steering, *Nat. Commun.* 7 (2016) 11480.
- [34] K. Steiner, W. Chen, A. Pasquarello, Band offsets of lattice-matched semiconductor heterojunctions through hybrid functionals and G₀W₀, *Phys. Rev. B* 89 (2014), 205309.
- [35] Y. Guo, J. Nan, Y. Xu, F. Cui, W. Shi, Y. Zhu, Thermodynamic and dynamic dual regulation Bi₂O₃/CO₂/Bi₂O₃/I enabling high-flux photogenerated charge migration for enhanced visible-light-driven photocatalysis, *J. Mater. Chem. A* 8 (2020) 8.
- [36] T. Lu, F. Chen, Multiwfn: a multifunctional wavefunction analyzer, *J. Comput. Chem.* 33 (2012) 580–592.
- [37] X. Bai, C. Sun, S. Wu, Y. Zhu, Enhancement of photocatalytic performance via a P3HT-g-C₃N₄ heterojunction, *J. Mater. Chem. A* 3 (2015) 2741–2747.
- [38] D. Zhao, Y. Wang, C.-L. Dong, Y.-C. Huang, J. Chen, F. Xue, S. Shen, L. Guo, Boron-doped nitrogen-deficient carbon nitride-based Z-scheme heterostructures for photocatalytic overall water splitting, *Nat. Energy* 6 (2021) 388–397.
- [39] J. Ag Pierre Lefebvre, Bernard Gil, and Henry Mathieu, Time-resolved photoluminescence as a probe of internal electric fields in GaN-(GaAl)N quantum wells, *Phys. Rev. B* 59 (1999) 5.
- [40] H.K. Jin Seo Im, J. Off, A. Sohmer, F. Scholz, A. Hangleiter, Reduction of oscillator strength due to piezoelectric fields in GaN/AlxGa1-xN quantum wells, *Phys. Rev. B* 57 (1997) 3.

- [41] G. Morello, F. Della Sala, L. Carbone, L. Manna, G. Maruccio, R. Cingolani, M. De Giorgi, Intrinsic optical nonlinearity in colloidal seeded grown CdSe/CdS nanostructures: Photoinduced screening of the internal electric field, *Phys. Rev. B* 78 (2008) 8.
- [42] Y. Hu, Y. Pan, Z. Wang, T. Lin, Y. Gao, B. Luo, H. Hu, F. Fan, G. Liu, L. Wang, Lattice distortion induced internal electric field in TiO₂ photoelectrode for efficient charge separation and transfer, *Nat. Commun.* 11 (2020) 2129.
- [43] X.J. Chen, J. Wang, Y.Q. Chai, Z.J. Zhang, Y.F. Zhu, Efficient photocatalytic overall water splitting induced by the giant internal electric field of a g-C₃N₄/rGO/PDIP Z-scheme heterojunction, *Adv. Mater.* 33 (2021) 7.
- [44] Z. Zhang, X. Chen, H. Zhang, W. Liu, W. Zhu, Y. Zhu, A highly crystalline perylene imide polymer with the robust built-in electric field for efficient photocatalytic water oxidation, *Adv. Mater.* 32 (2020), e1907746.
- [45] F. Steiner, J. Vogelsang, J.M. Lupton, Singlet-triplet annihilation limits exciton yield in poly(3-hexylthiophene), *Phys. Rev. Lett.* 112 (2014), 137402.
- [46] C. Chen, W. Ma, J. Zhao, Semiconductor-mediated photodegradation of pollutants under visible-light irradiation, *Chem. Soc. Rev.* 39 (2010) 4206–4219.
- [47] G. Li puma, Dimensionless analysis of photocatalytic reactors using suspended solid photocatalysts, *Chem. Eng. Res. Des.* 83 (2005) 820–826.
- [48] N.M. Reis, G. Li Puma, A novel microfluidic approach for extremely fast and efficient photochemical transformations in fluoropolymer microcapillary films, *Chem. Commun.* 51 (2015) 8414–8417.
- [49] D. Wang, M.A. Mueses, J.A.C. Márquez, F. Machuca-Martínez, I. Grčić, R. Peralta Muniz Moreira, G. Li, Puma, Engineering and modeling perspectives on photocatalytic reactors for water treatment, *Water Res.* 202 (2021), 117421.
- [50] Y. Li, Y. Fu, M. Zhu, Green synthesis of 3D tripyramid TiO₂ architectures with assistance of aloe extracts for highly efficient photocatalytic degradation of antibiotic ciprofloxacin, *Appl. Catal. B-Environ.* 260 (2020), 118149.
- [51] X. Wang, X. Wang, J. Huang, S. Li, A. Meng, Z. Li, Interfacial chemical bond and internal electric field modulated Z-scheme Sv-ZnIn₂S₄/MoSe₂ photocatalyst for efficient hydrogen evolution, *Nat. Commun.* 12 (2021) 4112.